

Accepted for publication in the Astrophysics Journal

## Numerical Modelling of Dusty Debris Disks

A. T. Deller and S. T. Maddison

*Centre for Astrophysics and Supercomputing, Swinburne University, PO Box 218, Hawthorn, VIC  
3122, AUSTRALIA*

### ABSTRACT

Infrared and submillimetre observations of nearby Vega-like stars have revealed a number of clumpy, asymmetric dust debris disks. Previous studies using semi-analytical and numerical methods have suggested planetary companions of various mass as the likely cause of most examples of disk asymmetry. In this paper, we modify an N-body symplectic gravitational integrator to include radiation terms and conduct medium-resolution parameter searches to identify likely planetary candidates in observed Vega-like systems. We also present high resolution models of Vega and  $\epsilon$  Eridani, comparing our results to those of previous authors, and a new model for Fomalhaut.

*Subject headings:* circumstellar matter – methods: N-body simulations – planetary systems – stars: individual (Vega,  $\epsilon$  Eridani, Fomalhaut)

### 1. Introduction

Dust disks composed of particles in the micron to centimetre range are known to exist around many stars that exhibit an infrared excess, such as Vega,  $\beta$  Pictoris,  $\epsilon$  Eridani and others (see e.g. Zuckerman 2001). Particles of this size are affected significantly by solar radiation and corpuscular (solar wind) forces, with Poynting-Robertson (PR) and solar wind drag resulting from the moving particle's absorption and reemission of solar energy. Over time, these dissipative forces caused by radiation and solar wind act to reduce a dust particle's semi-major axis and eccentricity, and the particle eventually spirals into the central star (Burns et al. 1979). Since the age of most of these systems exceeds the expected lifetime of a small dust particle, the particles must be continually replenished. The suspected mechanism is a collisional cascade involving primordial planetesimal and smaller sized bodies (Backman & Paresce 1993; Wyatt & Dent 2002) as is believed to occur in the Edgeworth-Kuiper Belt (e.g. Backman et al. 1995; Landgraf et al. 2002). The destructive process which leads to dust formation has led these disks to be known as 'debris disks'.

Of the debris disks near enough to Earth to be spatially resolved, most show a significant degree of asymmetry (e.g. Vega: Holland et al. 1998;  $\epsilon$  Eridani: Greaves et al. 1998). The commonly

held view is that gravitational interactions with an unseen embedded planet are responsible for most cases of disk structure (Ozernoy et al. 2000; Quillen & Thorndike 2002; Wilner et al. 2002). Alternative possible explanations have been considered for specific systems, such as disturbance by a passing star (e.g. HD141569: Clampin et al. 2003), a recent large cometary/planetesimal collision (e.g. Fomalhaut: Wyatt & Dent 2002) and contamination by a background feature such as a distant galaxy (e.g. Vega: Wilner et al. 2002).

A planetary companion has several effects on an initially uniform debris disk. Particles near the planet are often ejected due to a close encounter – an effect which is enhanced as the planet’s mass increases. Since particles interior to the planet spiral increasingly rapidly into the central star, an interior cleared zone is usually present (Liou & Zook 1999). However, some particles spiralling in towards the star may become trapped in a series of Mean Motion Resonances (MMRs) with the planet. An MMR exists when the ratio of orbital periods for two objects orbiting a central mass is equal to  $m : n$ , where  $m$  and  $n$  are integers. The order of an MMR is given by the quantity  $|m - n|$ . Earth has a dust ring formed by dust particles in MMRs (Dermott et al. 1994), and Neptune is suspected to do the same to Kuiper Belt dust (Liou & Zook 1999).

Whilst locked into an MMR with a planet, the angular momentum of the particle lost to Poynting-Robertson and solar wind drag is balanced by the resonant forcing of the planet’s gravitation. A particle trapped in an MMR can extend the particle’s lifetime to many times the value predicted by Poynting-Robertson and solar wind drag alone. The resultant ‘pile-up’ of particles at discrete semi-major axes tends to cause prominent radial and angular structure in the debris disk (Kuchner & Holman 2003).

In multiple planet systems, it is the outermost planet that generally dominates the structure of the resulting debris disk. Neptune is suspected to play this role in interactions with Kuiper Belt dust (Liou & Zook 1999). The interior planets, however, can have significant effects on particles which ‘leak past’ the outermost planet. In the solar system, for example, Jupiter and Saturn eject many dust particles which drift interior to Neptune (Liou & Zook 1999). For simplicity, we investigate only single planet systems and assume that the effects of any interior planets which may be present is negligible outside the orbit of the outermost planet.

In this paper, we numerically simulate a large number of debris disk systems, creating a synthetic debris disk catalogue. Our numerical method is described in Section 2, and the testing of the code is detailed in Section 3. We present a small sample of the results from the synthetic catalogue in Section 4, and use the catalogue to select planetary configurations which could be responsible for the observed systems of Vega,  $\epsilon$  Eridani and Fomalhaut. The selected systems are then simulated in higher detail in Section 5, and the results compared to observational data. Our conclusions are presented in Section 6.

## 2. Numerical Method

We model the evolution of debris disks using an N-body integrator that includes the effects of radiation pressure, Poynting-Robertson and solar wind drag. In this section we discuss the modifications made to a symplectic integrator to account for the additional forces, as well as our numerical techniques for creating debris disks and recording particle positions.

### 2.1. The RMVS3 Integrator

Since the general problem of a particle moving under the influence of gravitational and radiation forces is nonlinear, it is necessary to numerically integrate the orbits of all particles. Commonly used integrators include Runge-Kutter, Burlisch-Stoer and Mixed Variable Symplectic (MVS) algorithms. The MVS integrator developed by Wisdom & Holman (1991) is normally the fastest, but has the disadvantage of being unable to follow close encounters between particles and planets, which are crucial to debris disk evolution. This drawback has been overcome with the use of integrators such as RMVS3 (Levison & Duncan 1994) and SyMBA (Duncan et al. 1998), which are based on the Wisdom & Holman (1991) scheme but can integrate close encounters. In this work we have modified RMVS3 to include radiation and solar wind forces which affect debris disk particles. Such an approach was used by Moro-Martin & Malhotra (2002), who modify a variant of SyMBA. (Note that SyMBA and RMVS3 handle close encounters between particles and planets in different ways.)

RMVS3 assumes that test particles are both massless and collisionless – the problem of dust collisions is discussed in Section 4.1. The code requires units such that the gravitational constant  $G = 1$  and so we have chosen distance, time and mass units to be 1 AU, 1 year and  $M_{\odot}/(4\pi^2)$  respectively. Throughout this paper we shall use  $a$  for the semi-major axis,  $e$  for eccentricity, and  $i$  for inclination, with the subscripts  $tp$ ,  $pb$  and  $pl$  referring to a test particle, parent body and planet respectively.

As developed in Wisdom & Holman (1991) and described in Levison & Duncan (1994), RMVS3 expands the Hamiltonian of a test particle into two integrable components given by

$$H = H_{kep} + H_{dist} , \quad (1)$$

where  $H_{kep}$  represents the Keplerian motion around the central star, and  $H_{dist}$  represents the perturbances on a test particle resulting from the planet(s). Using a timestep  $\Delta t$ , the second order approximation implemented in RMVS3 consists of applying the disturbance Hamiltonian for  $\Delta t/2$ , applying the Keplerian Hamiltonian for  $\Delta t$ , and then applying the disturbance Hamiltonian again for  $\Delta t/2$ . The approximation is accurate as long as the planetary disturbances are small compared to the Keplerian evolution. This assumption of small disturbances does not hold when a particle suffers a close encounter with a planet. In this situation, since the gravitational effect of the planet on the particle exceeds that of the star, the roles of planet and star are reversed and the Keplerian

portion of the Hamiltonian is taken to occur around the planet and the star is relegated to the role of disturbance Levison & Duncan (1994). Although a smaller timestep is used during a close encounter, the duration of an encounter is typically small enough that the simulation proceeds rapidly. In the intermediate region where planetary and stellar forces are comparable, the timestep is also reduced but the integration remains heliocentric.

## 2.2. Addition of Radiation and Solar Wind

The magnitude of the radiation force on a particle is given by

$$|F_{rad}| = \frac{LAQ_{PR}}{4\pi cr^2}, \quad (2)$$

where  $L$  is stellar luminosity,  $A$  is the particle cross-sectional area,  $Q_{PR}$  is the radiation pressure coefficient,  $c$  is the speed of light and  $r$  is the heliocentric distance. It is standard practice to describe the strength of the radiation force on a given particle as a fraction of the gravitational force on a particle, such that

$$F_{rad} = \beta F_{grav}. \quad (3)$$

The constant  $\beta$  depends on the particle size and composition, as well as the stellar mass and luminosity, but is independent of the particle’s heliocentric distance. The magnitude of Poynting-Robertson drag is proportional to  $\beta$ . The ratio of solar wind drag to Poynting-Robertson drag is dependent on particle size, but is relatively constant over the range of particles usually considered ( $s > 0.5\mu\text{m}$ , Burns et al. 1979), so the combined drag effects of PR and solar wind can be expressed using a single parameter given by

$$\beta_{sw} = \beta(1 + sw), \quad (4)$$

where  $sw$  is the ratio of solar wind drag to Poynting-Robertson drag (Burns et al. 1979). Following Moro-Martin & Malhotra (2002), we use a constant value of  $sw = 0.35$  in all our simulations.

The acceleration on a particle due to solar wind drag and radiation, ignoring terms of order  $(v/c)^2$  and higher, is given by

$$\frac{d^2\mathbf{r}}{dt^2} = F_{grav} \left[ \beta\hat{\mathbf{r}} - \frac{\beta_{sw}}{c} (v_r\hat{\mathbf{r}} + \mathbf{v}) \right]. \quad (5)$$

The first term in this expression is the result of the outwardly-directed radiation pressure, which causes the net acceleration in the radial direction to be reduced to  $(1 - \beta)F_{grav}$ . The remaining two terms (which are smaller by a factor of  $v/c$ ) represent the Poynting-Robertson and solar wind drag. Poynting-Robertson drag results from the particle’s motion relative to the radiation source, which causes a component of the radiation force to oppose the particle’s motion. During normal particle movement, the first term is accounted for in the Keplerian Hamiltonian by reducing the central object mass to the ‘apparent’ value, while the other terms are added to the disturbance Hamiltonian. During a close encounter with a planet, the entire expression is added to the disturbance Hamiltonian.

### 2.3. Particle Initialisation

All simulations commence with a central star, an orbiting planet and a number of test particles distributed around the star with a fixed value of  $\beta$ . The star is fixed at the origin and has mass represented by  $M_\star$ . The orbiting planet is described by  $M_{pl}$ ,  $a_{pl}$  and  $e_{pl}$ , representing the planet’s mass, semi-major axis and eccentricity respectively.

Test particles are assumed to be released from larger ‘parent bodies’ (which are unaffected by radiation pressure) at the beginning of the simulation. This is analogous to the creation of dust through the collision of larger rocky bodies in a debris disk. The concept of a parent body is used only to set initial orbital parameters for test particles; they play no part in the simulation after initialisation. For each simulation, the initial distribution of parent bodies is specified by a range of semi-major axis, eccentricity and inclination values, given by  $a_{pb}$ ,  $e_{pb}$  and  $i_{pb}$  respectively. The arguments of perihelion, longitudes of ascending nodes and mean anomalies for the parent bodies are allocated randomly. A test particle is then created from each parent body, with semi-major axis, eccentricity and inclination referred to by  $a_{tp}$ ,  $e_{tp}$  and  $i_{tp}$  respectively. Since the test particles are affected by radiation pressure while the parent bodies are not, the test particles will have different orbital parameters from their parent bodies. In particular, the test particles will have increased semi-major axes and changed eccentricities, given by

$$a_{tp} = a_{pb} \frac{1 - \beta}{1 - 2a_{pb}\beta/r}, \quad (6)$$

$$e_{tp} = \left( 1 - \frac{(1 - 2a_{pb}\beta/r)(1 - e_{pb}^2)}{(1 - \beta)^2} \right)^{1/2}. \quad (7)$$

### 2.4. Particle Recording

Simulating a sufficient number of test particles to resolve the disk structure at all times is computationally expensive and an alternative method, used by Liou & Zook (1999) and Moro-Martin & Malhotra (2002), is to simulate a smaller number of particles and regularly record their positions, which can then be summed to produce distribution maps. A simulation is terminated after a fixed time or when all particles have been destroyed through either ejection via close encounters with planets or accretion onto the central star. In this way, long lived particles (trapped in resonances) contribute more to the final dust distribution. If we assume the dust distribution is ergodic and that the total dust mass is constant (i.e. the dust production rate equals the loss rate), this approach should give an accurate representation of the actual ‘steady-state’ disk structure.

In previous studies (e.g. Moro-Martin & Malhotra 2002) the particle locations have been transformed into a reference frame which rotates with the outermost planet, but this approach is not appropriate for planets with eccentric orbits. For this reason, we instead ensure that the particle

recording takes place with the planet in specific orbital phases. In this way a number of ‘snapshots’ of the system are taken with the planet in varying locations, allowing the effect of planetary phase to be studied (Wilner et al. 2002; Kuchner & Holman 2003). For example, many simulations utilised a planet with orbital period 300 years and a particle recording time of 1000 years, resulting in particle distributions for three different planetary phases.

It should be noted that there are some limitations to this procedure of simulating a debris disk using a small number of test particles. As discussed by Moro-Martin & Malhotra (2002), because both the probability of being trapped in a particular resonance and the time spent in a resonance depend sensitively on initial conditions, using a limited number of particles may over-exaggerate the importance of a particular resonance. We have tried to overcome this problem by using an order of magnitude more particles than previous simulations (e.g. Quillen & Thorndike 2002; Moro-Martin & Malhotra 2002) in high resolution simulations (see following sections). An additional problem with this procedure is that all of the test particles are released from their parent body at the same time, with a specific planetary phase. In reality, dust particles would be released continuously, at random planetary phases. This effect, however, is not likely to have a significant impact, since the test particles are typically released a long way from the planet and are distributed randomly around the star.

Setting a fixed maximum simulation time may also be problematic. For the small particle number approach to be accurate, the integration should be continued until all test particles have been destroyed. The termination of a simulation at a predetermined time means that some particles may still be active at the end of the simulation. One could argue, however, that extremely long-lived particles are unlikely to exist due to destruction via particle collisions. Since RMVS3 is a collisionless code, the destruction of particles in this way is not accounted for. We investigate these effects in more detail in Section 4.1.

### 3. Test Calculations

There is no general solution for the motion of a particle under the influence of radiation and gravitational forces in a system comprising a star and one or more planets. However, analytic solutions and analytic approximations exist for particle motion in the two-body (Wyatt & Whipple 1950) and the circularly restricted three-body (Liou & Zook 1997) problems respectively. These specific cases can be used to check the accuracy of the modified RMVS3 code.

To ensure that the addition of radiation and solar wind forces did not effect the normal running of the code, we ran a series of tests in which  $\beta$  was set to zero, and compared the results to identical tests run using the original RMVS3. The results were indistinguishable in all cases.

### 3.1. The 2-body problem

The time rate of change of a test particle’s orbital elements in the radiation-modified two body problem are given in Moro-Martin & Malhotra (2002) (following the work of Wyatt & Whipple (1950); Burns et al. (1979)), and are equal to

$$\left(\frac{da}{dt}\right) = -\frac{(1+sw)\beta M_\star}{c} \frac{(2+3e^2)}{a(1-e^2)^{3/2}}, \quad (8)$$

$$\left(\frac{de}{dt}\right) = -\frac{5(1+sw)\beta M_\star}{2c} \frac{e}{a^2(1-e^2)^{1/2}}, \quad (9)$$

$$\left(\frac{di}{dt}\right) = 0. \quad (10)$$

where  $M_\star$  is the mass of the central star, and  $c$  is the speed of light.

To test the code against the two-body solutions, we ran a simulation with a single  $\beta = 0.15$  test particle placed in orbit around a solar-mass star, released from a parent body with  $a_{pb} = 250$  AU,  $e_{pb} = 0.8$  and  $i_{pb} = 7.6^\circ$ . The particle’s argument of perihelion, longitude of ascending node and mean anomaly were selected randomly. The analytical and numerical results plotted in Figure 1 are in excellent agreement.

### 3.2. The restricted 3-body problem

The addition of a planet greatly complicates the motion of the test particle, but Liou & Zook (1997) have derived expressions for the time evolution of a particle’s orbital elements whilst in an MMR with a zero eccentricity planet. These expressions are a second order approximation, valid only for low test particle eccentricities and inclinations, and low order resonances, and are given by

$$e^2 = (e_0^2 - (K-1)/3) \exp(3At/K) + (K-1)/3, \quad (11)$$

$$i = i_0 \exp(-At/4), \quad (12)$$

where  $A = (2\beta_{sw}M_\star)/(a^2c)$ ,  $K = m/n$ ,  $e_0$  and  $i_0$  represent the particle’s initial eccentricity and inclination, and  $m$  and  $n$  are the integers specifying the resonance. It should be noted that the location of resonances is shifted from their normal location due to the presence of the radiation force, which causes particles at a given semi-major axis to orbit more slowly due to the reduced effective gravitational force. The semi-major axis of a particle locked in an  $m : n$  resonance with a planet is given by

$$a_{tp} = a_{pl} (1 - \beta)^{1/3} (m/n)^{2/3}. \quad (13)$$

We start at time  $t = 0$  with a single particle placed exterior to the resonance in orbit around a one solar mass star and a planet at 30 AU. We follow the orbital evolution of the test particle as it passes through the MMR until it is ejected from the system, and compare the results with

equations 11 and 12. We show the results for two different  $\beta$  values. In Figure 2a, a single  $\beta = 0.05$  particle is trapped in a 3 : 2 resonance with a Neptune mass planet, while in Figure 2b a particle with  $\beta = 0.2$  is trapped in a 2 : 1 resonance with a Jupiter mass planet. The particles’ orbital elements are well described until their eccentricity and inclination become too large and the analytic solution becomes invalid. The results shown in Figure 2 are only a small sample of the large number of tests carried out to ensure the accuracy of the code.

#### 4. A Synthetic Debris Disk Catalogue

Previous studies by Kuchner & Holman (2003) have predicted the general effects of varying planetary mass and eccentricity on the dust distribution in a debris disk. We have generated a synthetic catalogue of debris disks which provides numerical agreement to the theoretical predictions and can be used as a guide when interpreting observed systems. Here, we present a sample of results obtained from modelling over 300 disks, showing the effects of planetary mass and eccentricity, dust composition ( $\beta$ ) and initial dust distribution on the disk structure. By generating simulated observations of these simulations, we show that even observations at a low resolution can distinguish between different planet and dust combinations.

For the creation of our synthetic catalogue, we allowed five parameters to vary:  $M_{pl}$ ,  $e_{pl}$ ,  $\beta$ ,  $a_{pb}$  and  $e_{pb}$ . All other parameters were fixed as follows:  $M_{\star} = 1M_{\odot}$ ,  $0^{\circ} < i_{pb} < 8^{\circ}$ ,  $n_{tp} = 500$ , and planetary period = 300 years (yielding  $a_{pl} \sim 44.8$  AU). Table 1 summarises the parameter space we have investigated. Of the 600 possible combinations of our five free parameters, approximately 300 disks were simulated. Subsets of the parameter space which were fully explored include  $\beta = 0.1$ ,  $M_{pl} = 0.05M_{Jup}$  and  $M_{pl} = 1M_{Jup}$ .



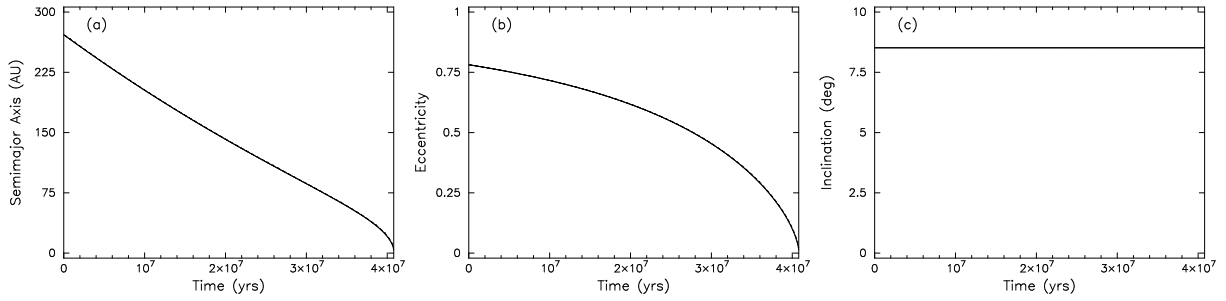


Fig. 1.— Time evolution of a single test particle orbiting a solar mass star subject to Poynting-Robertson and solar wind drag. Plotted are the evolution of (a)  $a_{tp}$ , (b)  $e_{tp}$ , and (c)  $i_{tp}$  for a particle with  $\beta = 0.15$  and  $sw = 0.35$ . The analytic solution (dashed line) and actual particle path (solid line) are coincident.

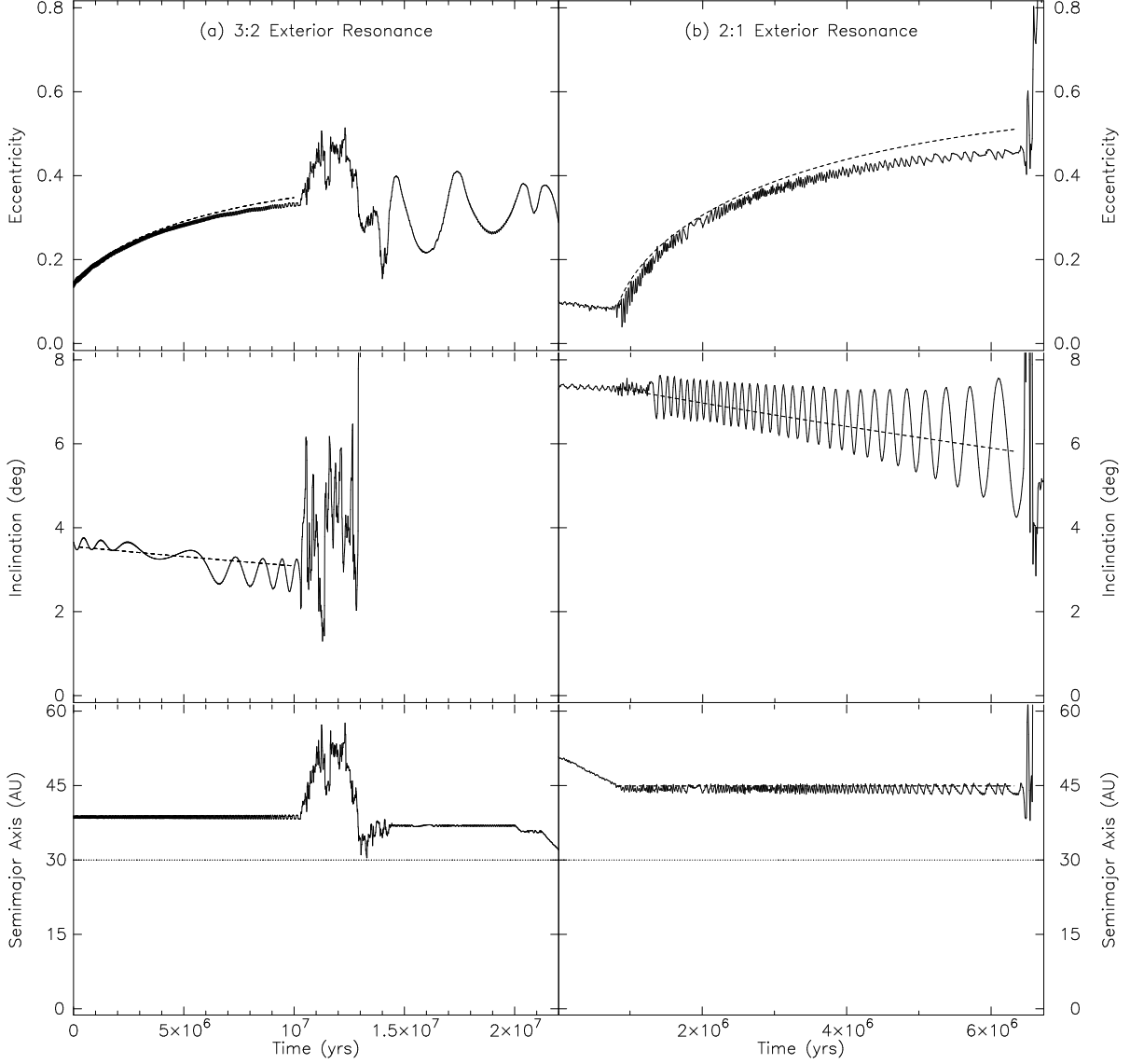


Fig. 2.— Evolution of a single test particle whilst in an MMR with a planet. The particle evolution is shown as a solid line, and the analytic solution is shown as a dashed line. The planetary semi-major axis is shown as a dotted line in the bottom two panels. (a) Particle with  $\beta = 0.05$ , in a 3:2 resonance with a  $0.05M_{Jup}$  mass planet. The particle is trapped for about  $10^7$  years. (b) Particle with  $\beta = 0.2$ , in a 2:1 resonance with a Jupiter mass planet. The particle is trapped for about 5 million years. In both cases  $sw = 0.35$ .

$\mathbf{M}_{pl}/M_{Jup}$	$\mathbf{e}_{pl}$	$\beta$	$a_{pb}/a_{pl}$	$e_{pb}$
			$[a_{min}, a_{max}]$	$[e_{min}, e_{max}]$
0.01	0.0	0.01	[1.0, 1.4] (close)	[0.0, 0.2] (low)
0.05	0.1	0.1	[1.4, 2.0] (mid)	[0.1, 0.5] (medium)
0.2	0.3	0.2	[2.0, 3.5] (far)	
1.0	0.5	0.4		
3.0	0.7			

Table 1: The range of parameter values used in generating our synthetic catalogue. Note that while this parameter space was not completely explored, approximately 300 of the 600 possible disks were simulated. Fully explored parameters (where the chosen parameter was simulated with all possible combinations of the other parameters) include  $\beta = 0.1$ ,  $M_{pl} = 0.05M_{Jup}$  and  $M_{pl} = 1M_{Jup}$ .

Each simulation was run for  $6 \times 10^7$  years, corresponding to  $2 \times 10^5$  planetary orbits. Particle positions were recorded every 1000 years, allowing observation of the system in 3 different planetary phases. The maximum and minimum allowable heliocentric radii of the test particles were 700 and 2 AU respectively.

At the end of each simulation, the recorded particle positions (in the three orbital phases) were binned in the  $XY$ -plane. The particle distribution in the  $XY$ -plane was then plotted for each particular planetary phase. We also binned particle semi-major axes and plotted the semi-major axis occupancy versus semi-major axis, which shows the location and strength of MMRs with the planet.

In order to produce synthetic observations of the systems, the particle distribution plots were weighted by estimated total disk mass and the dust emissivity at  $850 \mu\text{m}$ , assuming the dust to be a perfect blackbody. This emissivity plot was then convolved with a two dimensional Gaussian with a full width half maximum (FWHM) of 40 AU, to simulate observations of the system with limited resolution. The synthetic observations can also be plotted from various disk viewing angles. This procedure assumes that the disk is optically thin, which is a reasonable assumption for disks containing little to no gas, as is the case for most Vega-like systems (Liseau 1999).

The complete synthetic catalogue is available for viewing online<sup>1</sup>. Here we present a sample of results from our catalogue for Jupiter and Neptune mass planets with  $e_{pl} = 0.1$  and  $0.5$  in Figures 3 and 4. These simulations use  $\beta = 0.1$ , and test particles released from parent bodies with orbital elements  $0 < e_{pb} < 0.2$ ,  $1.4 < a_{pb}/a_{pl} < 2.0$  and  $0 < i_{pb} < 8^\circ$ .

As can be seen in Figures 3 and 4, the mass and eccentricity of a planet dramatically alters the resulting dust distribution. The Jupiter-mass planet clears a central cavity, which is not as pronounced in the Neptune-mass case. In the low planetary eccentricity case, a relatively smooth dust ring is present external to the planet. When the planetary eccentricity is increased, the smooth ring vanishes, replaced by prominent arcs or clumps of dust emission. Similar trends were observed in the synthetic catalogue with planets of different masses. These results closely resemble the predictions made by Kuchner & Holman (2003) for the four cases of: (a) low mass, low eccentricity planets, (b) low mass, moderate eccentricity planets, (c) high mass, low eccentricity planets, and (d) high mass, moderate eccentricity planets.

Figure 5 shows the resonance occupations for the  $e_{pl} = 0.1$  cases. The effect of planetary mass is again highlighted, with a high mass planet trapping particles in a few strong resonances, mostly at higher semi-major axes, while a low mass planet has many weaker resonances, closer to the planet’s semi-major axis. More accurate simulated observations for specific systems and telescopes are undertaken in Section 5.

---

<sup>1</sup><http://astronomy.swin.edu.au/debrisdisk/>

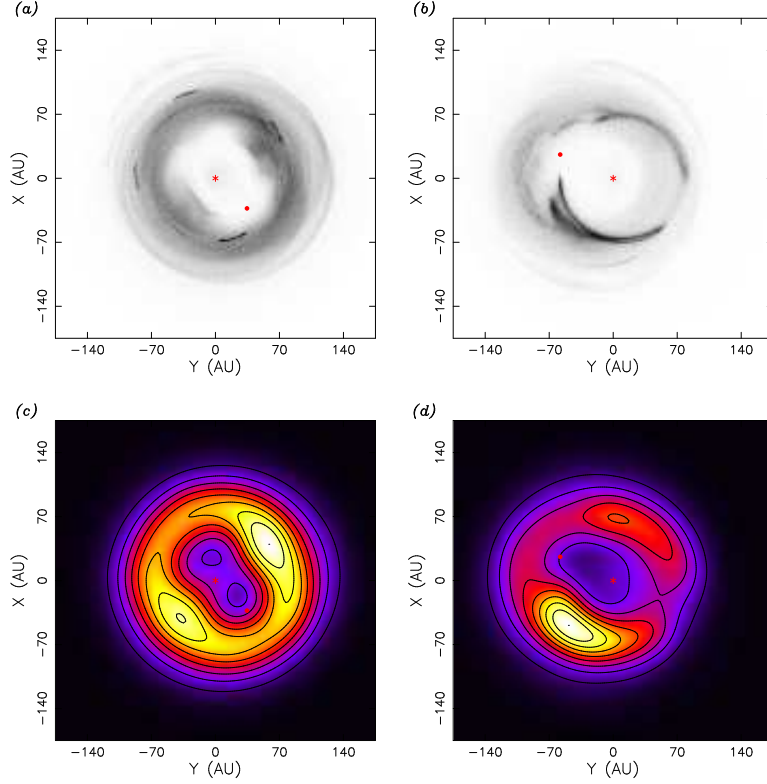


Fig. 3.— Simulations of a system containing a single Jupiter mass planet and 500 test particles after  $6 \times 10^7$  years, or 20,000 orbital periods. In each case, the planet is located at  $a_{pl} \sim 44.8$  AU, test particles were released from parent bodies with  $1.4 < a_{pb}/a_{pl} < 2.0$ ,  $0 < e_{pb} < 0.2$  and  $0 < i_{pb} < 8^\circ$  and  $\beta = 0.1$ . The star and planet are represented by a filled star and circle respectively (coloured red in the online edition of the Journal). Plots (a) and (b) show the dust distributions generated when  $e_{pl} = 0.1$  and  $0.5$  respectively. Plots (c) and (d) show simulated observations of the disks (with beam FWHM 40 AU) for  $e_{pl} = 0.1$  and  $0.5$  respectively. See the electronic edition of the Journal for a colour version of this figure.

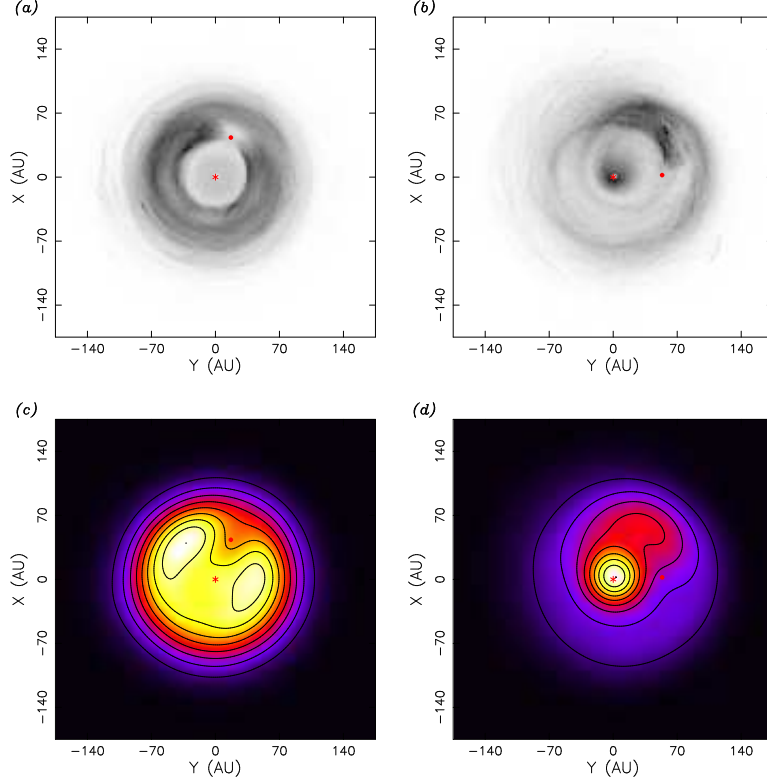


Fig. 4.— Simulations of a system containing a single Neptune mass planet and 500 test particles after  $6 \times 10^7$  years, or 20,000 orbital periods. In each case, the planet is located at  $a_{pl} \sim 44.8$  AU, test particles were released from parent bodies with  $1.4 < a_{pb}/a_{pl} < 2.0$ ,  $0 < e_{pb} < 0.2$  and  $0 < i_{pb} < 8^\circ$  and  $\beta = 0.1$ . Plots (a) and (b) show the dust distributions generated when  $e_{pl} = 0.1$  and  $0.5$  respectively. Plots (c) and (d) show simulated observations of the disks (with beam FWHM 40 AU) for  $e_{pl} = 0.1$  and  $0.5$  respectively. See the electronic edition of the Journal for a colour version of this figure.

#### 4.1. Dust Lifetime and Collisional Processes

As discussed in Section 2.4, our numerical procedure of using a small number of particles can lead to potential problems when terminating the simulation at a specified time, as some long-lived particles may still be active. In a real debris disk, however, grain collisions would limit the maximum lifetime of particles.

In Figure 6 we show the results of a simulation of a Jupiter mass planet with  $a_{pl} \sim 44.8$  AU and  $e_{pl} = 0.5$  system containing 500 test particles with  $\beta = 0.1$ . The test particles are released from parent bodies with  $1.4 < a_{pb}/a_{pl} < 2.0$ ,  $0.0 < e_{pb} < 0.2$  and  $0.0^\circ < i_{pb} < 8.0^\circ$ . The three panels show the dust distribution when the simulation is terminated after 11.7 million years, 40 million years and 153 million years, corresponding to 10%, 2% and 0% of particles remaining active. It can be seen that the basic disk structure is created rapidly, and the final few particles have a limited impact despite having lifetimes many times the median. The longest-lived particles tend to ‘sharpen’ the distribution and bring out finer detail, which is hidden in our simulated observations (telescope FWHM 40 AU). Thus, the imposition of a cut-off lifetime (whether as a numerical convenience or as a substitute for dust destruction through collisions) is of little consequence as long as most (>90%) particles have already been accreted or ejected.

### 5. Modelling Observed Systems

In this section we use the synthetic disk catalogue to select planetary configurations which generate structures similar to the observed debris disk systems Vega,  $\epsilon$  Eridani and Fomalhaut. We then optimise the planetary and parent body parameters, and increase the resolution (by increasing the number of test particles) to produce more accurate synthetic observations, which we compare to previous observational and numerical studies of these three debris disk systems.

#### 5.1. Vega

Vega ( $\alpha$  Lyrae) was the first star identified with an infrared excess associated with a disk of dusty material (Aumann et al. 1984) and has become the prototype for so-called ‘Vega-type’ stars. Subsequent observations with SCUBA (Holland et al. 1998) and the IRAM Plateau de Bure Interferometer (Wilner et al. 2002) confirm that Vega is surrounded by a dusty disk, with two prominent clumps of emission. Wilner et al. (2002) proposed that the twin lobes of emission seen in these images are caused by dust trapped in MMRs with a massive, eccentric planet ( $M_{pl} = 3M_{Jup}$ ,  $e_{pl} = 0.6$ ) orbiting Vega with a semi-major axis of 40 AU. In their model, the initial test particle longitudes of perihelion were constrained to be aligned closely with the planet’s longitude of perihelion (which is reasonable for a high eccentricity system). They also noted that a wide variety of planetary parameters can produce the twin-lobed structure seen in Vega.

Whilst our code was able to reproduce the results of Wilner et al. (2002), their synthetic observations (at the resolution of the Holland et al. (1998) Vega observations) show nearly symmetrical emission, whereas the Holland et al. (1998) observations show a significant asymmetry. (It should be noted, however, that there are uncertainties in the Holland et al. (1998) observations. In the model we are about to present, we are assuming that the observed asymmetry is real.) Based on results from our synthetic catalogue, we have modelled Vega using an entirely different planetary configuration in an attempt to better match these observations. In our model, a more distant ( $a_{pl} = 73.7$  AU), less eccentric ( $e_{pl} = 0.1$ ) 3 Jupiter mass planet reproduces the observed disk structure, with no constraints on the initial test particle perihelia (since we are modelling a lower eccentricity planet). We use 5000 test particles released from parent bodies with initial orbital elements in the range  $90 < a_{pb} < 120$ ,  $0.0 < e_{pb} < 0.3$ , and  $0^\circ < i_{pb} < 8^\circ$ .

Dent et al. (2000) state that to fit the observed spectral energy distribution, the dust grains which make up the Vega disk must have diameters in the range 60–400  $\mu\text{m}$ , corresponding to  $\beta = 0.02 - 0.11$  for Vega’s estimated mass and luminosity. We have simulated this system with  $\beta$  values of 0.02, 0.05 and 0.1, and found negligible differences between the synthetic observations. (Note that Wilner et al. (2002) used  $\beta = 0.01$  with  $sw = 0$ .) Figure 7 shows the dust distribution, simulated observation and resonance occupancy plots obtained using our Vega model with  $\beta = 0.05$ .

We note that our model for Vega produces a dust distribution which is essentially stationary in the planet’s frame of reference. Such a distribution means that as the planet orbits the star, observations from Earth will show positional changes in the emission peaks over an orbital timescale. Dust distributions from the four orbital phases recorded are shown in Figure 8.

The model accurately reproduces the twin lobes seen in the Wilner et al. (2002) observations, as well as the extended emission seen in the lower resolution Holland et al. (1998) observations. Figure 7a shows asymmetry in the two emission features, which are not collinear with the star nor the same distance from the star, as seen in the Wilner et al. (2002) observations. This model also provides reasonable constraints on the orbital parameters of the proposed planet; for example, the same model with  $e_{pl} = 0.2$  results in a markedly different structure, as does a significantly less massive ( $M_{pl} < M_{Jup}$ ) planet. The primary concern with this model is the requirement that such a massive planet have formed or migrated to such a large distance from the central star, although the fact that Vega is estimated to be 2.5 times as massive as the sun may mitigate this problem. Future detailed observations are required to test our planetary model.

## 5.2. $\epsilon$ Eridani

First identified as a Vega-type star in 1984 (Aumann 1985),  $\epsilon$  Eridani has been the subject of ongoing planetary speculation since disk images taken at 850  $\mu\text{m}$  by Greaves et al. (1998) showed a clumpy, asymmetric ring, with a cleared region interior to  $\sim 30$  AU. Radial velocity observations by Hatzes et al. (2000) detected a  $1.7M_{Jup}$  planetary companion with  $a \sim 3.4$  AU and  $e_{pl} \sim 0.6$ .



Such a close companion, however, cannot account for the observed disk structure seen by Greaves et al.

Numerical simulations by Ozernoy et al. (2000) have suggested the presence of a  $M_{pl} = 0.2M_{Jup}$ ,  $a_{pl} = 55 - 65$  AU,  $e_{pl} = 0.0$  planet, while Quillen & Thorndike (2002) proposed a  $M_{pl} = 0.1M_{Jup}$ ,  $a_{pl} = 41.6$  AU,  $e_{pl} = 0.3$  planet in the  $\epsilon$  Eridani disk. A planet with mass equal to or greater than Jupiter is unlikely to be responsible for the observed disk structure, since massive planets tend to trap particles in the  $n : 1$  resonances (Kuchner & Holman 2003). Our simulations of a Jupiter mass planet, shown in Figure 9a, demonstrate this effect. For particles to occupy the  $n + 1 : n$  resonances near a massive planet, their parent bodies must also reside very close to the planet, and in this situation most particles are quickly scattered or ‘leak past’ the planet, as shown in Figure 9b. This results in a structure which lacks the observed central cavity of  $\epsilon$  Eridani (see Figure 9c and 9d). The presence of the observed central clearing would then require the gravitational influence of a second, more massive planet at an intermediate semi-major axis (Liou & Zook 1999).

Ozernoy et al. consider only particles in the 2:1 and 3:2 resonances (in equal proportions), while Quillen & Thorndike consider only particles with  $a_{tp} = [1.1, 1.5]a_{pl}$ . An examination of our results shows why; if particles with semi-major axes smaller than the semi-major axis of the planet are allowed (as in Figure 10a), emission from particles close to the star dominates and a ring structure is not seen (see Figure 10b). The implied ejection of particles from the inner regions of the disk hints at another undiscovered and more massive planet at an intermediate distance from the star. The requirements for such a planet are discussed below.

We suggest that the system proposed by Ozernoy et al. is unlikely to be responsible for the  $\epsilon$  Eridani disk for two reasons: (1) their model is symmetrical whereas the original observations by Greaves et al. (1998) and subsequent  $350 \mu\text{m}$  observations by D. J. Wilner (2004, private communication) state that only the most prominent clump (in the southeast of the image) is definitely present, and (2) our simulations show that dust released in a range encompassing the 2:1 and 3:2 resonances will always occupy other resonances such as the 5:3, and that the resonance occupancies are rarely in equal proportion. We therefore investigate the model proposed by Quillen & Thorndike in more detail.

Our models differ somewhat from those of Quillen & Thorndike in that we use 5000 test particles (increasing the resolution by an order of magnitude), we include solar wind drag, and model the system in three dimensions. The simulations were terminated after  $3 \times 10^8$  years, when less than 1% of the test particles remained active. Because the dominant grain size in the  $\epsilon$  Eridani disk has not been well determined, we have simulated the system using two  $\beta$  values,  $\beta = 0.1$  and  $0.01$ . Initial parent body semi-major axes and eccentricities are set in the range  $[1.1 a_{pl}, 1.5 a_{pl}]$  and  $[0, 0.4]$  respectively, while initial inclinations are in the range  $[0^\circ, 8^\circ]$ . Our results are shown in Figure 10.

Both the  $\beta = 0.1$  and  $\beta = 0.01$  models reproduce the ring structure seen in the sub-mm

observations, possessing a single prominent emission maxima and one or more secondary maxima. As expected, the contrast and detail is higher in the  $\beta = 0.01$  case, since more particles are trapped in resonances for longer. Unlike Vega, this dust distribution generated by this model is not fixed in the planet’s reference frame, but the emission peaks do show positional changes over a planetary orbit, as shown in Figure 11. Our results confirm the model proposed by Quillen & Thorndike (2002) as a viable explanation for the  $\epsilon$  Eridani system, with the caveat that an additional massive body must exist interior to the dust-sculpting planet’s orbit.

In order to confirm that an inner planet is responsible for clearing the inner regions of the disk, one would like to simply introduce a second planet into the  $\epsilon$  Eridani model. However, since the introduction of a second planet introduces variations into the orbital elements of the primary outer planet, recording particle positions with the outer planet in an fixed position over time is no longer possible. We can instead introduce an inner planet to our model at a range of semi-major axes and make use of test particle occupancy versus semi-major axis plots to determine if the inner planet effectively removes particles from the inner  $\sim 40$  AU of the system.

Plots of occupancy versus semi-major axis are shown in Figure 12 for our preferred model of  $\epsilon$  Eridani (Figure 12a) and models including the addition of a second, Jupiter mass planet with  $e_{pl} = 0.3$  at three different semi-major axes;  $a_{pl} = 10, 15$  and  $18$  AU (Figure 12b, 12c, and 12d). We see that the addition of a Jupiter mass planet with a semi-major axis between  $10 - 18$  AU is capable of substantially reducing particle occupation of semi-major axes less than that of the exterior planet. We found that a planet located too far from the star ( $a_{pl} \geq 20$  AU) disrupted the orbit of the outer planet and resulted in a dynamically unstable system. Note the change in the scaling of the graphs in Figure 12. We can clearly see that when an inner planet is included, the resonance occupancy decreases, reflecting a reduction in particle lifetimes. An understanding of the exact effects of a massive inner planet will have to await detailed simulations with large particle numbers, which can resolve the disk at all times. Such an investigation is planned for a future paper.

### 5.3. Fomalhaut

Unlike the previous systems, Fomalhaut has not yet been subject to detailed numerical simulations. The Fomalhaut system also differs markedly in that  $850 \mu\text{m}$  SCUBA observations suggest the system is seen nearly edge-on and consists of a dusty torus, rather than a thin disk (Holland et al. 1998). The improved spatial resolution offered by the  $450 \mu\text{m}$  SCUBA images of Holland et al. (2003) confirm the torus structure, while revealing a previously unseen arc of emission near or within the torus. This departure from a uniform structure is strongly suggestive of a planetary presence.

The generation of a single arc of emission can be achieved by a 1:1 resonance, as suggested by Holland et al. (2003). Inspection of results for resonance occupancy obtained in the construction

of our synthetic catalogue, however, indicate that the 1:1 resonance is difficult to populate under normal circumstances. An example is shown in Figure 13, where a Jupiter mass planet populates the 1:1 resonance when parent bodies exist interior to the planet, but does not populate the 1:1 resonance when the parent bodies are all external to the planet. We consider it unlikely that parent bodies with semi-major axes slightly less than the planet’s semi-major axis would survive for the required length of time. As an alternative explanation of the single arc feature, we find that systems including a massive ( $M_{pl} \geq M_{Jup}$ ), moderately eccentric ( $0.3 \leq e_{pl} \leq 0.5$ ) planet can induce a single emission arc over a background ring by trapping many particles in the  $n : 1$  resonances, where  $n > 1$ .

After examining our synthetic catalogue, we chose a model with the following parameters:  $M_{\star} = 2.3M_{\odot}$  (appropriate for an A3V star such as Fomalhaut – Barrado y Navascues et al. 1997),  $M_{pl} = 2M_{Jup}$ ,  $e_{pl} = 0.4$ , and  $a_{pl} \sim 59$  AU. Parent bodies were distributed with initial orbital parameters in the following ranges:  $0 < e_{pb} < 0.3$ ,  $100 < a_{pb} < 180$  AU,  $0 < i_{pb} < 25^{\circ}$ . The higher parent body inclinations naturally generates a torus structure, which is believed to exist in the Fomalhaut system. The simulation used 1000 test particles with  $\beta = 0.05$ , since the mass of dust grains in the Fomalhaut system with diameters  $> 100\mu\text{m}$  (corresponding to values of  $\beta > 0.1$ ) is believed to be negligible (Dent et al. 2000). The results of our simulations, which ran until no particles remained after 212 million years, are shown in Figure 14. The simulated observations bear a close resemblance to the ‘raw’  $450\mu\text{m}$  image of Fomalhaut presented in Holland et al. (2003).

This planetary configuration does generates a dust distribution which does not rotate with the planet, but appears fixed from a viewpoint external to the system over an orbital period. Thus, observations of Fomalhaut over time would show no change in emission if this model is correct. The effects of planetary phase are shown in Figure 15.

Whilst the planetary configuration we have presented here displays a close similarity to the observations of Fomalhaut to date, as noted above results from our synthetic catalogue suggest that several parameters from the model may be varied slightly whilst still producing similar results. The semi-major axis of the planet is well constrained by the location of the dust ring, but the the production of a single arc of emission is seen with several combinations of massive, moderate eccentricity planets. Thus, this model is only representative of a class of planetary configurations which could be responsible for the structure seen in the Fomalhaut disk.

## 6. Conclusions

We have modified an N-body symplectic integrator to include the effects of Poynting-Robertson and solar wind drag in order to model collisionless debris disks, and used the modified integrator to produce a synthetic disk catalogue containing approximately 300 model disks. The catalogue has two applications: the comparison of theoretical predictions of disk structure to numerical results, and to give an idea of the parameter space which might satisfy a particular observed system,

possibly identifying planets which are presently undetectable through Doppler shift techniques. Using this synthetic catalogue as a guide, we have produced ‘best fit’ models for three observed debris disk systems whose disk structures can be explained by the presence of a planetary companion or companions.

We have modelled Vega using a planet with  $M_{pl} = 3M_{Jup}$ ,  $a_{pl} = 73.7$  AU and  $e_{pl} = 0.1$ . The dust distribution generated by this model rotates with the planet, meaning future observations of Vega should show changes in spatial dust emission as the planetary phase changes. However, since a range of planetary parameters can produce the dust distribution inferred for the Vega system, our solution is representative of that produced by a class of massive ( $M_{pl} > M_{Jup}$ ), low eccentricity ( $e_{pl} < 0.2$ ) planetary companions.

$\epsilon$  Eridani was modelled using a planet with  $M_{pl} = 0.1M_{Jup}$ ,  $a_{pl} = 41.6$  AU and  $e_{pl} = 0.3$ , a model first proposed by Quillen & Thorndike (2002). Although the dust distribution generated by this model does not rotate with the planet, it does change over the course of an orbital period, offering hope for confirmation by future observations. However, this model is dependent on the existence of a second, massive inner planet to clear particles interior to the modelled planet, which cannot be simulated using the techniques outlined in this paper.

We modelled Fomalhaut using a planet with  $M_{pl} = 2M_{Jup}$ ,  $a_{pl} = 59$  AU and  $e_{pl} = 0.4$ . The dust distribution generated by this model does not change significantly over the course of a planetary orbit, and thus the effect of planetary phase would be difficult to detect in future observations. Like the model presented for Vega, our model for Fomalhaut is the best match to current observations from a class of massive, moderate eccentricity planets which generate similar structure.

Numerical modelling of planets in dusty debris disks has shown that planets which are undetectable through present techniques are likely to be responsible for the observed asymmetries of known debris disk systems. It should be noted, however, that it is difficult to positively identify a unique planetary companion without temporal information showing the changes in disk structure over the course of a planetary orbit.

The authors wish to thank Hal Levison for useful discussions about RMVS3 and Dave Wilner for providing an unpublished 350  $\mu\text{m}$   $\epsilon$  Eridani image. We also thank the anonymous referee for providing useful feedback and suggestions. AD was supported by a Summer Vacation Scholarship from the Swinburne Centre for Astrophysics and Supercomputing. All simulations were run on the Swinburne supercomputer<sup>2</sup>.

Our synthetic debris disk catalogue is available online at:  
<http://astronomy.swin.edu.au/debrisdisks/>

---

<sup>2</sup><http://supercomputing.swin.edu.au/>

## REFERENCES

- Aumann, H. H. et al. 1984, ApJ, 278, L23
- Aumann, H. H. 1984, PASP, 97, 885
- Backman, D. E. & Paresce, F. 1993, in Protostars and Planets III, ed. E.H. Levy & J.I. Lunine (University of Arizona Press), 1253
- Backman, D. E., Dasgupta, A. & Stencel, R. E. 1995, ApJ, 450, L35
- Barrado y Navascues, D., Stauffer, J. R., Hartmann, L. & Balachandran, S. C. 1997, ApJ, 475, 313
- Burns, J. A., Lamy, P. L. & Soter, S. 1979, Icarus, 40, 1
- Clampin, M. et al. 2003, AJ, 126, 385
- Dent, W. R. F., Walker, H. J., Holland, W. S. & Greaves, J. S. 2000, MNRAS, 314, 702
- Dermott, S. F., Jayaraman, S., Xu, Y. L., Gustafson, B. A. S. & Liou, J.-C. 1994, Nature, 369, 719
- Duncan, M. J., Levison, H. F. & Lee, M. H. 1998, AJ, 116, 2067
- Greaves, J. S. et al. 1998, ApJ, 506, L133
- Hatzes, A. P. et al. 2000, ApJ, 544, L145
- Holland, W. S. et al. 1998, Nature, 392, 788
- Holland, W. S. et al. 2003, ApJ, 582, 1141
- Kuchner, M. J. & Holman, M. J. 2003, ApJ, 588, 1110
- Landgraf, M., Liou, J.-C., Zook, H. A. & Grün, E. 2002, AJ, 123, 2857
- Levison, H. F. & Duncan M. J. 1994, Icarus, 108, 18
- Liou, J.-C. & Zook, H. A. 1997, Icarus, 128, 354
- Liou, J.-C. & Zook, H. A. 1999, AJ, 118, 580
- Liseau, R. 1999, A&A, 348, 133
- Moro-Martin, A. & Malhotra, R. 2002, AJ, 124, 2305
- Ozernoy, L. M., Gorkavyi, N. N., Mather, J. C., & Taidakova, T. A. 2000, ApJ, 537, L147
- Quillen, A. C., & Thorndike S. 2002, ApJ, 578, L149
- Wilner, D. J., Holman, M. J., Kuchner, M. J., & Ho, P. T. P. 2002, ApJ, 569, L115

Wisdom, J. & Holman, M. 1991, AJ, 102, 1528

Wyatt, M. C. & Dent, W. R. F. 2002, MNRAS, 334, 589

Wyatt, S. P. & Whipple, F. L. 1950, ApJ, 111, 134

Zuckerman, B. 2001, ARA&A, 39, 549

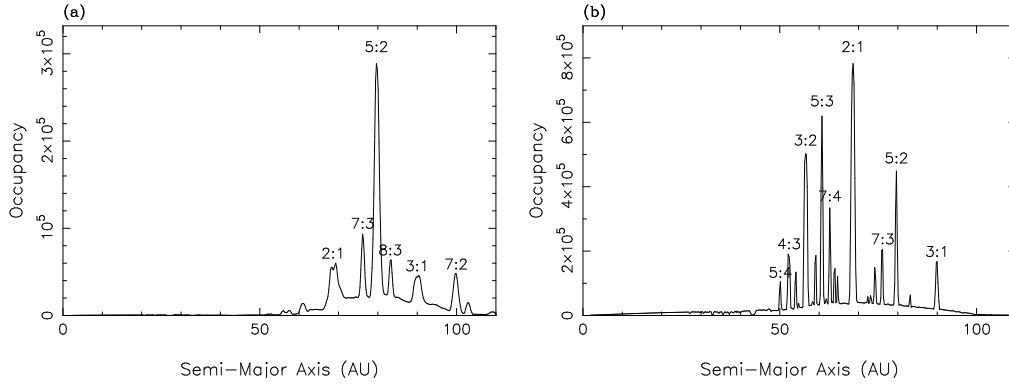


Fig. 5.— Resonance occupation for a system containing a single planet with (a)  $M_{pl} = M_{Jup}$ , (b)  $M_{pl} = 0.05 M_{Jup}$ . In each case, the planet has  $e_{pl} = 0.1$  and  $a_{pl} \sim 44.8$  AU. Note the lower mass planet tends to trap particles in narrower resonances, closer to the planet’s semi-major axis.

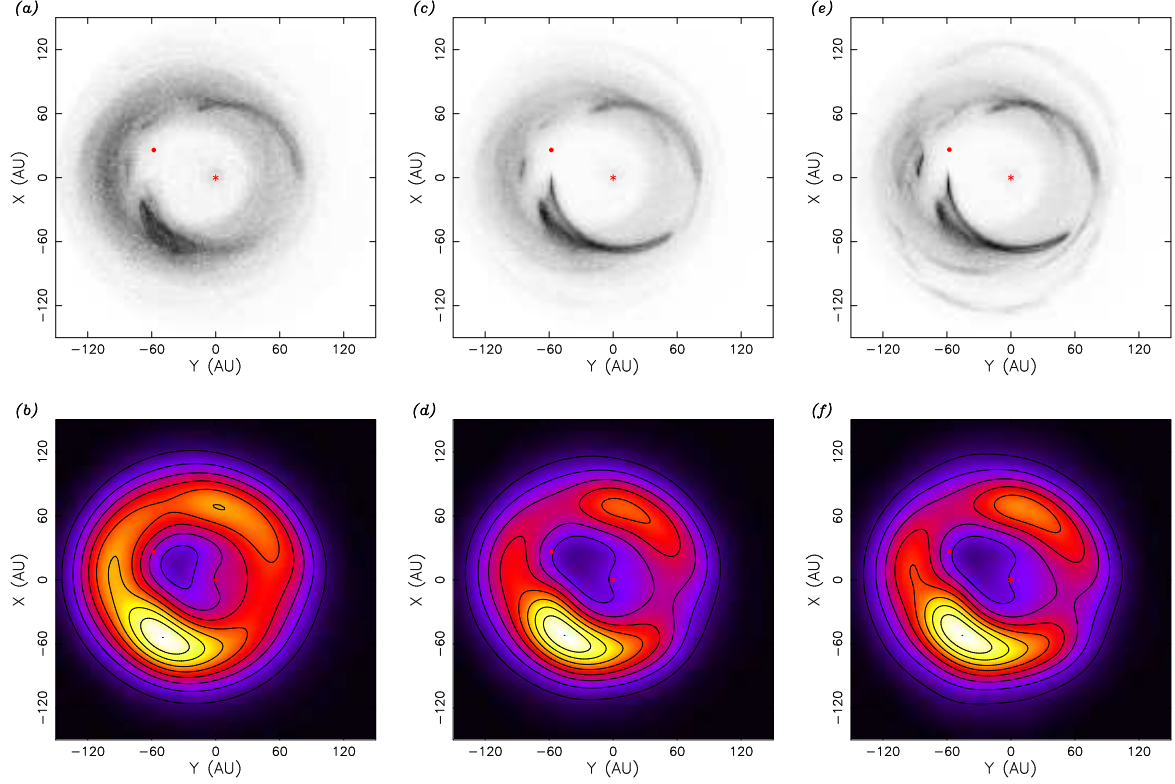


Fig. 6.— Integrated dust distribution from a system containing a Jupiter mass planet with eccentricity 0.5 and semi-major axis 44.8 AU, and 500 test particles with  $\beta = 0.1$ . Parent bodies had initial orbital elements  $1.4 < a_{pb}/a_{pl} < 2.0$ ,  $0.0 < e_{pb} < 0.2$  and  $0.0^\circ < i_{pb} < 8.0^\circ$ . Simulated observations utilised a 2D Gaussian with FWHM of 40 AU. Plots (a) and (b) show the dust distribution and a simulated observation after 11.7 million years (10% of particles remaining). Plots (c) and (d) show distribution and simulated observation after 40 million years (2% of particles remaining). Plots (e) and (f) show distribution and simulated observation after 153 million years (no particles remaining). See the electronic edition of the Journal for a colour version of this figure.



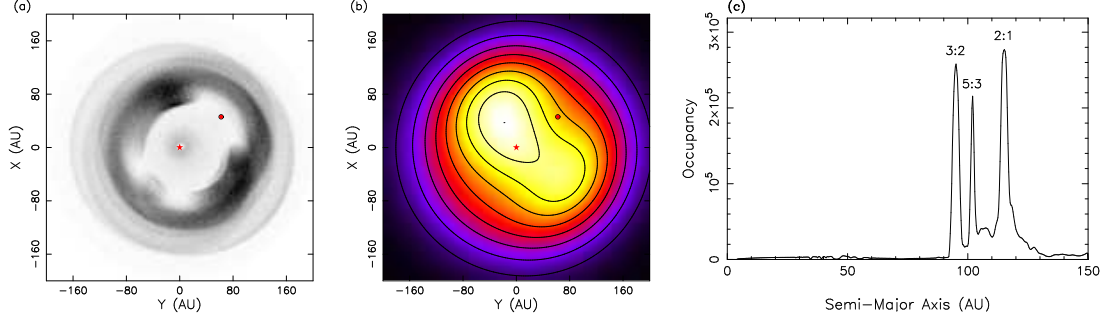


Fig. 7.— Results of Vega simulation using  $a_{pl} = 73.7$  AU,  $e_{pl} = 0.1$  and 5000 test particles with  $\beta = 0.05$  released from parent bodies with  $90 < a_{pb} < 120$  AU,  $0.0 < e_{pb} < 0.3$ , and  $0^\circ < i_{pb} < 8^\circ$ . The simulation was terminated after  $10^8$  years with 0.6% of particles remaining. (a) Dust distribution – note the two peaks as seen in the Wilner et al. (2002) interferometric observations. (b) Simulated observation of the system using a resolution of 108 AU (equal to the resolution of the  $850 \mu\text{m}$  SCUBA observations by Holland et al. 1998) and a 5 mJy solar flux, with contours at 2 mJy separation. The two peaks merge together at low resolution, although one dominates slightly. (c) Resonance occupancy in the Vega model. See the electronic edition of the Journal for a colour version of this figure.

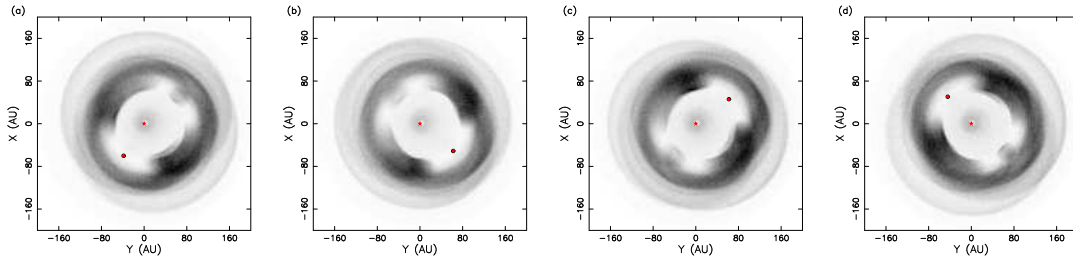


Fig. 8.— Dust distribution generated by the Vega simulations (with  $\beta = 0.05$ ) at the four different recorded planetary phases. The distribution rotates with the planet, meaning observations from Earth will show positional changes in the emission peaks over the planetary period.

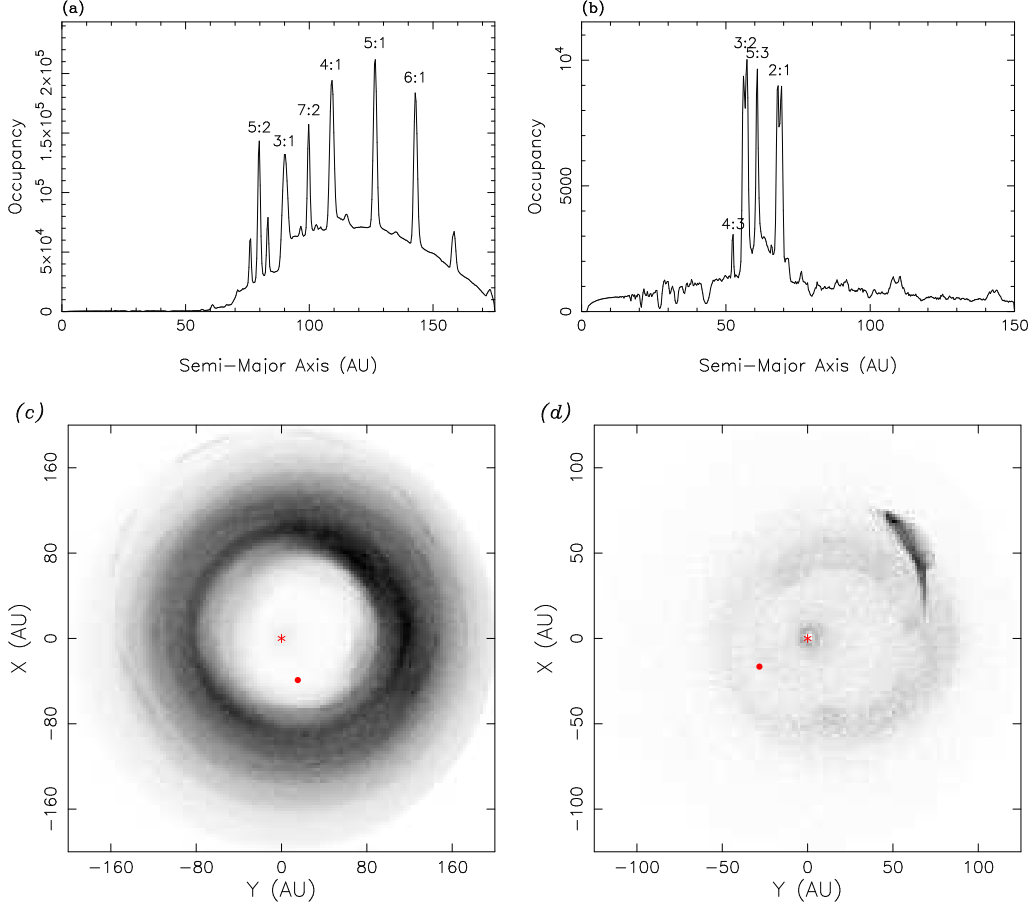


Fig. 9.— Structures resulting from a Jupiter mass planet with  $a_{pl} \sim 44.8$  AU and  $e_{pl} = 0.3$ . Test particles have  $\beta = 0.1$ , and are released from parent bodies with initial eccentricity range  $e_{pb} = [0.0, 0.2]$ . (a) Resonance occupancy when the initial range of  $a_{pb}$  is  $[2.0, 3.5]a_{pl}$ . The higher order  $n:1$  resonances dominate. Note the high number of total particle positions recorded, indicating longer average particle lifetimes. (b) Resonance occupancy when the initial range of  $a_{pb}$  is  $[1.0, 1.4]a_{pl}$ . The planet rapidly removes test particles, and only a few resonances close to the planet’s semi-major axis are populated. (c) The dust distribution created when the initial range for  $a_{pb}$  is  $[2.0, 3.5]a_{pl}$ . A distinct ring structure is formed, containing two (unequal) density enhancements. (d) The dust distribution created when the initial range for  $a_{pb}$  is  $[1.0, 1.4]a_{pl}$ . A ring structure is not generated

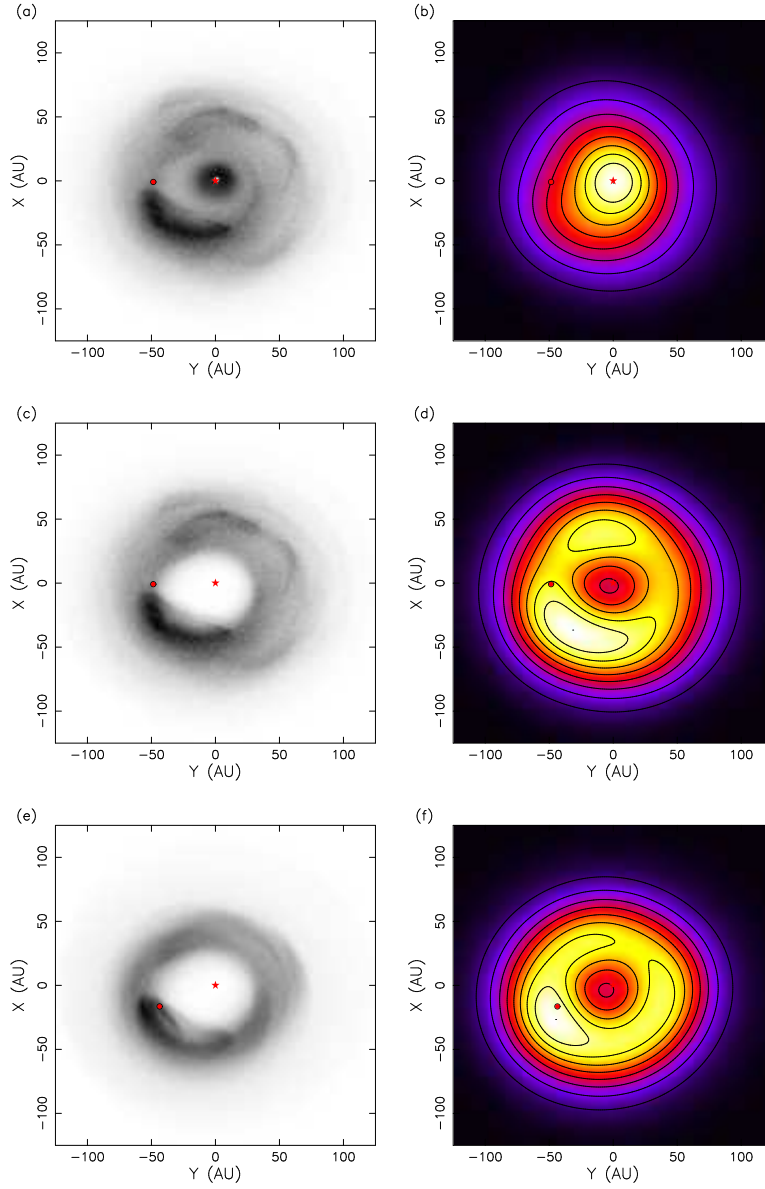


Fig. 10.— Simulations of  $\epsilon$  Eridani including a  $M_{pl} = 0.1M_{Jup}$ ,  $e_{pl} = 0.3$  planet with a semi-major axis of 41.6 AU, from a viewing angle of  $30^\circ$ . Parent bodies had  $1.1 < a_{pb}/a_{pl} < 1.5$ ,  $0 < e_{pb} < 0.3$  and  $0.0 < i_{pb} < 8.0$ . The telescope beam FWHM was set to 45 AU - the approximate beam diameter of the Greaves et al. (1998) images. (a) Dust distribution,  $\beta = 0.1$ , all particles allowed. (b) Simulated observation,  $\beta = 0.1$ , all particles allowed. Emission close to the star dominates and the ring structure is faint. (c) Dust distribution,  $\beta = 0.1$ , particles with semi-major axes less than the planet removed. (d) Simulated observation,  $\beta = 0.1$ , particles with semi-major axes less than the planet removed. (e) Dust distribution,  $\beta = 0.01$ , particles with semi-major axes less than the planet removed. (f) Simulated observation,  $\beta = 0.01$ , particles with semi-major axes less than the planet removed. See the electronic edition of the Journal for a colour version of this figure.

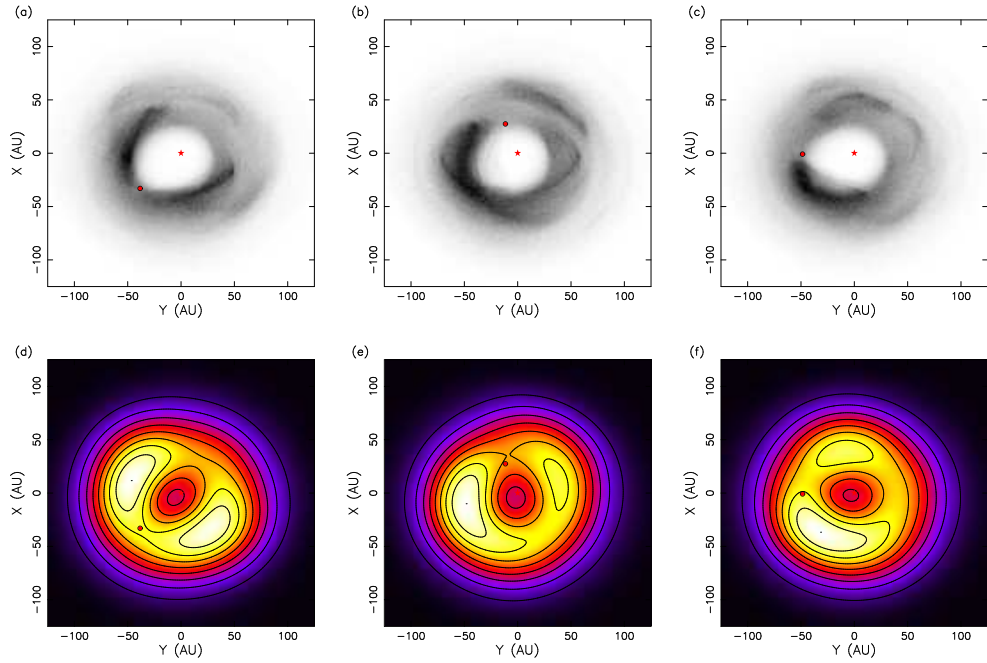


Fig. 11.— Dust distribution and synthetic observations from by the  $\epsilon$  Eridani simulations (with  $\beta = 0.1$  and particles with semi-major axes interior to the planet removed) at three different planetary phases. Dust distributions are shown in (a) to (c), with the corresponding synthetic observations shown in (d) to (f). The distribution does not rotate with the planet, but the emission peaks show positional changes over the course of an orbit. See the electronic edition of the Journal for a colour version of this figure.

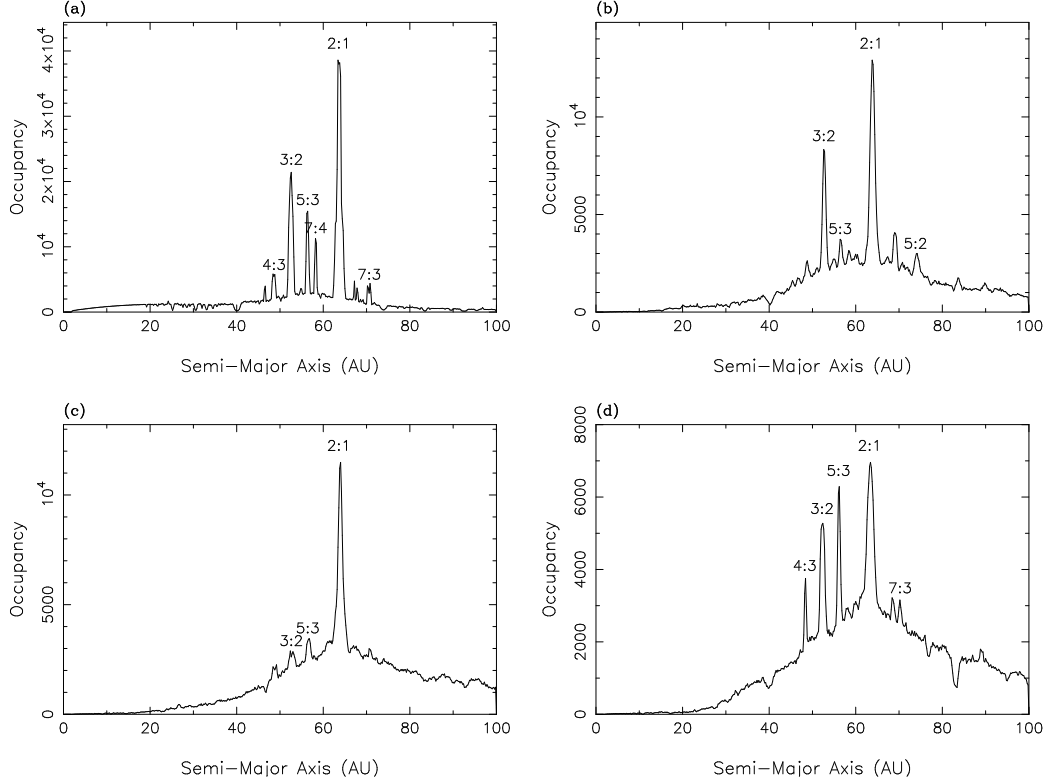


Fig. 12.— Occupancy versus semi-major axis plots showing the effect of adding a Jupiter mass,  $e_{pl} = 0.3$  inner planet to the  $\epsilon$  Eridani model. Plot (a) shows the plot for the unmodified  $\epsilon$  Eridani model - note test particles occupancy of semi-major axes interior to 40 AU. Plots (b), (c) and (d) show the results for systems with an inner planet added with a semi-major axis of 10, 15 and 18 AU respectively. In each case, test particle occupancy of semi-major axes interior to 40 AU is substantially reduced (note the different scales on the four graphs). Simulations contained five hundred  $\beta = 0.1$  test particles were released from parent bodies with  $46 < a_{pb} < 62$  AU,  $0.0 < e_{pb} < 0.4$  and  $0.0^\circ < i_{pb} < 8.0^\circ$  and were terminated after  $10^8$  years.

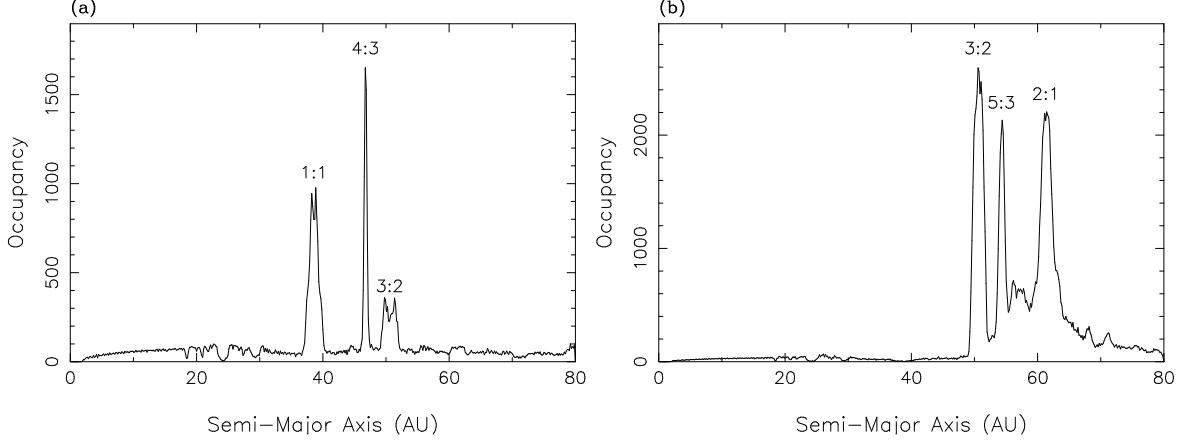


Fig. 13.— The resonance occupancy for a 500 particle simulation of a system containing a Jupiter mass planet with  $a_{pl} = 40$  AU and  $e_{pl} = 0.1$ . Test particles had  $\beta = 0.1$ . (a) With parent bodies in the range  $35 < a_{pb} < 45$  AU,  $0.0 < e_{pb} < 0.3$  and  $0.0^\circ < i_{pb} < 8.0^\circ$ , the 1:1 resonance is prominent. (b) When parent bodies are in the range  $45 < a_{pb} < 60$  AU,  $0.0 < e_{pb} < 0.3$  and  $0.0^\circ < i_{pb} < 8.0^\circ$ , there is no population of the 1:1 resonance.

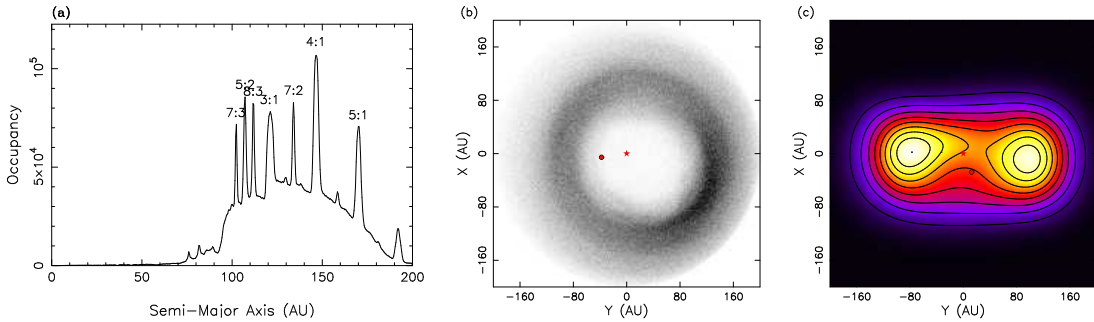


Fig. 14.— Simulations of the Fomalhaut system using a  $2 M_{Jup}$  planet with  $e_{pl} = 0.4$  and  $a_{pl} \sim 59$  AU. (a) The resonance occupation - note that the  $n:1$  resonances dominate. (b) Face-on distribution of particles. (c) Simulated observation of system at  $450\mu\text{m}$  from an inclination of  $70^\circ$ . The telescope FWHM of is 50 AU, equivalent to the resolution of SCUBA at  $450\mu\text{m}$ . Contours show equal intensity increments. See the electronic edition of the Journal for a colour version of this figure.

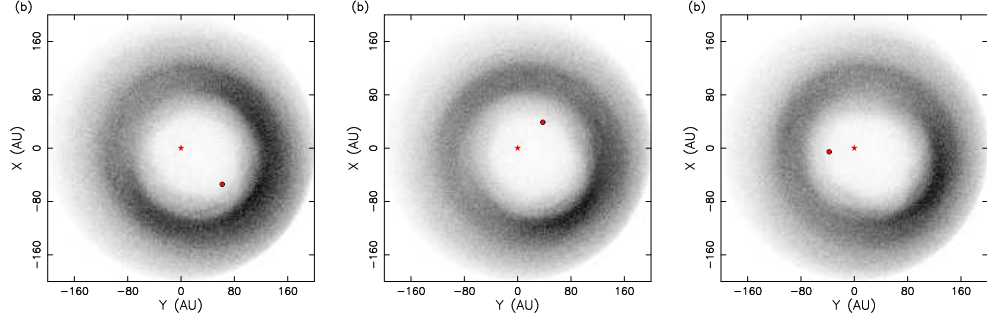


Fig. 15.— Dust distribution generated by the Fomalhaut simulations at three different planetary phases. The distribution does not rotate with the planet, and remains relatively constant in a fixed reference frame.